



Two-year Cosmology Large Angular Scale Surveyor (CLASS) Observations: A Measurement of Circular Polarization at 40 GHz

Ivan L. Padilla¹ , Joseph R. Eimer¹ , Yunyang Li (李云扬)¹ , Graeme E. Addison¹ , Aamir Ali^{1,2} , John W. Appel¹ , Charles L. Bennett¹ , Ricardo Bustos³ , Michael K. Brewer¹, Manwei Chan^{1,4} , David T. Chuss⁵ , Joseph Cleary¹, Jullianna Couto¹ , Sumit Dahal¹ , Kevin Denis⁶, Rolando Dünner⁷, Thomas Essinger-Hileman⁶ , Pedro Fluxá⁷ , Dominik Gothe¹, Saianeesh K. Haridas¹ , Kathleen Harrington^{1,8} , Jeffrey Iuliano¹, John Karakla¹, Tobias A. Marriage¹ , Nathan J. Miller^{1,6}, Carolina Núñez¹ , Lucas Parker^{1,9}, Matthew A. Petroff¹ , Rodrigo Reeves¹⁰, Karwan Rostem⁶ , Robert W. Stevens¹¹ , Deniz Augusto Nunes Valle¹, Duncan J. Watts¹ , Janet L. Weiland¹, Edward J. Wollack⁶ , and Zhilei Xu (徐智磊)^{1,12}

¹ Department of Physics and Astronomy, Johns Hopkins University, 3701 San Martin Drive, Baltimore, MD 21218, USA; padilla@jhu.edu

² Department of Physics, University of California, Berkeley, CA 94720, USA

³ Facultad de Ingeniería, Universidad Católica de la Santísima Concepción, Alonso de Ribera 2850, Concepción, Chile

⁴ Department of Aeronautics and Astronautics, Massachusetts Institute of Technology, 77 Massachusetts Avenue, Cambridge, MA 02139, USA

⁵ Department of Physics, Villanova University, 800 Lancaster Avenue, Villanova, PA 19085, USA

⁶ Goddard Space Flight Center, 8800 Greenbelt Road, Greenbelt, MD 20771, USA

⁷ Instituto de Astrofísica and Centro de Astro-Ingeniería, Facultad de Física, Pontificia Universidad Católica de Chile, Av. Vicuña Mackenna 4860, 7820436 Macul, Santiago, Chile

⁸ Department of Physics, University of Michigan, Ann Arbor, MI 48109, USA

⁹ Space and Remote Sensing, MS DB244, Los Alamos National Laboratory, Los Alamos, NM 87544, USA

¹⁰ CePIA, Departamento de Astronomía, Universidad de Concepción, Concepción, Chile

¹¹ National Institute of Standards and Technology, 325 Broadway, Boulder, CO 80305, USA

¹² Department of Physics and Astronomy, University of Pennsylvania, 209 South 33rd Street, Philadelphia, PA 19104, USA

Received 2019 November 1; revised 2019 December 9; accepted 2019 December 12; published 2020 January 29

Abstract

We report measurements of circular polarization from the first two years of observation with the 40 GHz polarimeter of the Cosmology Large Angular Scale Surveyor (CLASS). CLASS is conducting a multi-frequency survey covering 75% of the sky from the Atacama Desert designed to measure the cosmic microwave background (CMB) linear E and B polarization on angular scales $1^\circ \lesssim \theta \lesssim 90^\circ$, corresponding to a multipole range of $2 \leq \ell \lesssim 200$. The modulation technology enabling measurements of linear polarization at the largest angular scales from the ground, the Variable-delay Polarization Modulator, is uniquely designed to provide explicit sensitivity to circular polarization (Stokes V). We present a first detection of circularly polarized atmospheric emission at 40 GHz that is well described by a dipole with an amplitude of $124 \pm 4 \mu\text{K}$ when observed at an elevation of 45° , and discuss its potential impact on the recovery of linear polarization by CLASS. Filtering the atmospheric component, CLASS places a 95% confidence upper limit of $0.4 \mu\text{K}^2$ to $13.5 \mu\text{K}^2$ on $\ell(\ell+1)C_\ell^{VV}/(2\pi)$ for $1 \leq \ell \leq 120$, representing an improvement by two orders of magnitude over previous CMB limits.

Unified Astronomy Thesaurus concepts: Cosmic microwave background radiation (322); Early universe (435); Observational cosmology (1146); Astronomical instrumentation (799); Polarimeters (1277); Sky surveys (1464); Reionization (1383); Big Bang theory (152)

1. Introduction

The cosmic microwave background (CMB) anisotropy, in intensity and linear polarization, has added excellent constraining power to modern cosmological models (Kovac et al. 2002; Netterfield et al. 2002; Bennett et al. 2013; Louis et al. 2017; Henning et al. 2018; Planck Collaboration et al. 2018). Standard cosmology and the Λ CDM model predict no significant primordial circular polarization, yet constraints on this prediction are sparse. Theoretical work has produced a variety of predictions of circularly polarized emission mechanisms. Synchrotron emission in galaxies is intrinsically elliptically polarized (Legg & Westfold 1968). Magnetized relativistic plasma in supernovae remnants of Population III stars (De & Tashiro 2015) and in galaxy clusters (Cooray et al. 2003) can convert E-mode polarization into circular polarization through Faraday conversion. Primordial magnetic fields can generate circular polarization in the CMB

(Giovannini 2009, 2010; Zarei et al. 2010). Circular polarization can result from coupling of the Chern–Simons term to electrodynamics, resulting in cosmic birefringence (Carroll et al. 1990). Other mechanisms for the production of circularly polarized emission are discussed in Ejlli (2019), Mohammadi (2013), Montero-Camacho & Hirata (2018), Inomata & Kamionkowski (2019), Kamionkowski (2018), Haghighat et al. (2019), Batebi et al. (2016), Motie & Xue (2011), Sawyer (2015), and Venumadhav et al. (2017), with a review in King & Lubin (2016). All predictions are still several orders of magnitude fainter than what is accessible with the sensitivity levels of current experiments. The brightest predicted source of circularly polarized emission is the Zeeman transition in atmospheric oxygen (Keating et al. 1998; Hanany & Rosenkranz 2003).

Upper limits on CMB circular polarization have been reported on scales of 8° – 24° by the Milano Polarimeter (MIPOL) at the level of $10^5 \mu\text{K}^2$ using a correlation receiver at

33 GHz (Mainini et al. 2013). The SPIDER balloon-borne experiment reported upper limits on scales $<10^\circ$ at the level of $10^2 \mu\text{K}^2$ (Nagy et al. 2017). The SPIDER measurement leveraged nonidealities in its half-wave plate polarization modulators, which provide indirect coupling to circular polarization, to produce an upper limit at 95 and 150 GHz. For comparison, these limits are three orders of magnitude larger than current linear polarization measurements (BICEP2 Collaboration et al. 2018). The SPIDER limits on extraterrestrial emission are a function of the source spectrum, and the limits are an order of magnitude better for a synchrotron-like emission mechanism with ν^{-3} scaling than for the CMB.

The Cosmology Large Angular Scale Surveyor (CLASS) is an array of four polarimetric telescopes situated in the Atacama Desert in Chile, operating at four frequencies spanning the microwave foreground minimum and targeting the polarized CMB at the largest angular scales (Eimer et al. 2012; Essinger-Hileman et al. 2014; Harrington et al. 2016). Making measurements of the sky at these scales will provide powerful constraints on the optical depth to the epoch of reionization (Watts et al. 2018) and cosmological inflationary models (Watts et al. 2015). The Variable-delay Polarization Modulator (VPM) technology employed by CLASS to access the largest scales provides explicit sensitivity to circular polarization (Section 2.1) (Chuss et al. 2012; Harrington et al. 2018). This same technology, operated cryogenically, is employed on the PIPER balloon-borne instrument (Gandilo et al. 2017). In comparison to coherent technologies, which can also directly measure circular polarization (Mainini et al. 2013), the CLASS strategy of coupling the free-space modulation of the VPM with subkelvin bolometric detectors can achieve higher sensitivity, especially at higher microwave frequencies. In contrast to the use of nonideal half-wave plates (Nagy et al. 2017), the VPM offers higher sensitivity to circular polarization that is not a function of the source spectrum. Throughout the rest of this work, we compare measurements on the basis of circular polarized emission with a CMB spectrum. CLASS has been observing 75% of the sky with the 40 GHz instrument since 2016, and the remaining frequencies of 90, 150, and 220 GHz have been deployed and are currently collecting data. We report on the results on circular polarization for the first two years of observation with the 40 GHz instrument over 56% of the sky.

In Section 2 we describe the data selection and analysis, including an explanation of the instrument’s coupling to circular polarization. In Section 3.1 we report on a first detection of circularly polarized atmospheric emission at 40 GHz and discuss its implications for the linear polarization measurements being made by CLASS. In Section 3.2 we present new upper limits on circularly polarized emission at 40 GHz.

2. Data Processing

2.1. Sensitivity to Circular Polarization

The CLASS front-end, fast modulation is provided by a VPM described in detail in Chuss et al. (2012) and Harrington et al. (2018). The VPM consists of a stationary grid of parallel wires that reflects light polarized along one axis and transmits light polarized along the other. The transmitted light reflects off a flat mirror behind the grid and recombines with light reflected by the grid with an optical path difference that depends on the

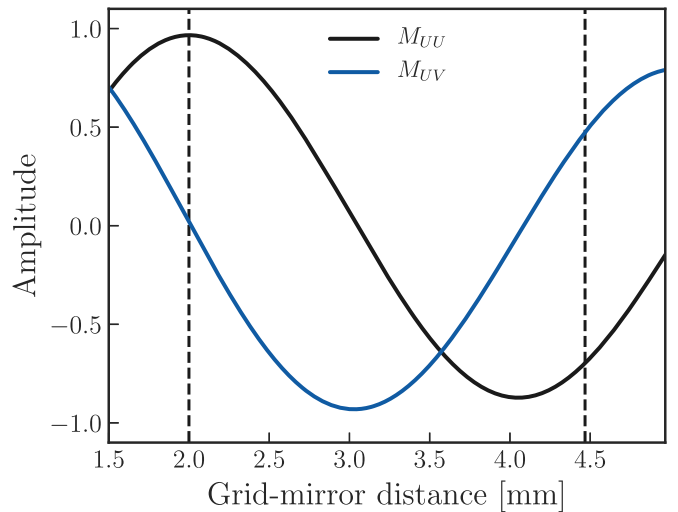


Figure 1. VPM modulation transfer functions for incident U and V polarization. The dashed vertical lines indicate the throw of the VPM for the 40 GHz instrument, through which Stokes U modulates into $-U$ through the Stokes V .

grid–mirror separation. The mirror is actuated to modulate the optical path difference at 10 Hz, moving the signal band to higher frequencies that are less vulnerable to $1/f$ and other low-frequency noise (Miller et al. 2016). During one cycle of operation, the VPM switches the Stokes parameter U for the incoming light into Stokes V , and then into Stokes $-U$ (Figure 1).

2.2. Mapmaking and Data Processing

The first era of CLASS observations ran from 2016 September through 2018 February. During this period, the 40 GHz instrument collected data year-round at a rate of 200 Hz with 64 polarization-sensitive bolometers (Appel et al. 2014, 2019). The telescope scans the sky by performing 720° azimuth “sweeps” in alternating directions, at a constant rate of one degree per second, held at an elevation of 45° . Each day the instrument observes at one of seven different boresight orientations, which range from -45° to $+45^\circ$ in increments of 15° . For this analysis we select data from the best 239 days of observation based on their noise properties, representing 62% of the total data collected. We discard data from detectors that performed poorly during the season, leaving a total of 57 bolometers. To identify and eliminate contamination of the data, we compute the variance of the timestream on windows of various lengths and apply cuts to regions with anomalous values. We apply an additional cut when the distance between a detector pointing and the Sun (Moon) is smaller than 20° (10°). The timestream calibration to thermal units is based on observations of the Moon and described in Appel et al. (2019). In the last pre-processing step we apply deconvolutions that correct for the readout filter (Battistelli et al. 2008), and time constants of the detectors.

The space between the grid and the mirror creates a resonant cavity that produces a signal that is a function of the grid–mirror separation, and the differential temperature and emissivity of the grid wires and the sky (Miller et al. 2016). To remove this VPM-synchronous signal we subtract a time-domain template created by averaging the data in each sweep in bins of grid position, as given by linear encoders on the VPM.

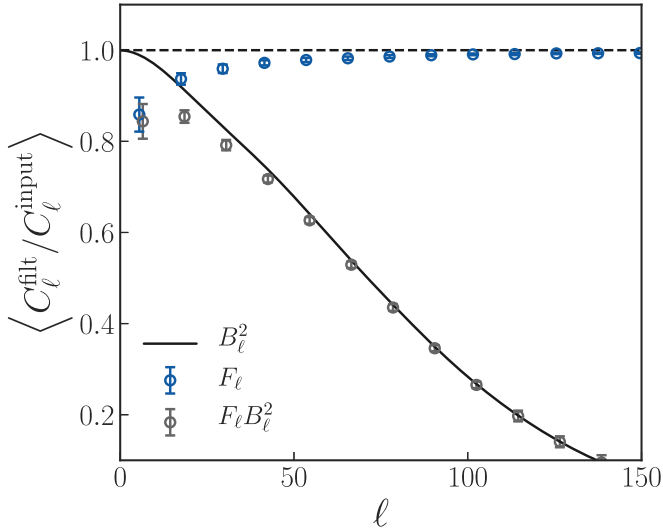


Figure 2. The mapmaking VV transfer function is shown in blue. The beam window function corresponding to the instrument’s 1.5° FWHM beam is shown as a solid black line. These two quantities determine the experiment’s sensitivity as a function of multipole. The gray points are the power spectrum window function $W_\ell = F_\ell B_\ell^2$. In this figure the points of the filter transfer function are artificially offset by $\Delta\ell = -1$ to aid visualization.

A model for the timestream data, d , obtained by multiplying the Mueller matrix of all elements in the optics chain, is

$$d = I + M_{UU}Q \cos(2\gamma) + M_{UU}U \sin(2\gamma) + M_{UV}V, \quad (1)$$

where γ is the sum of the parallactic angle of the grid and telescope boresight angle, and M_{ij} for $i, j \in \{I, Q, U, V\}$ are the elements of the 4×4 VPM Mueller matrix (Miller et al. 2016). These elements are a function of the grid–mirror separation z , $M_{ij} = M_{ij}(z)$. To produce a map, we invert this timestream model using the traditional linear least-squares mapmaking equation

$$s = (A^T N^{-1} A)^{-1} A^T N^{-1} d, \quad (2)$$

where s is an $N_{\text{pixels}} \times N_{\text{Stokes}}$ vector representing the sky maps of each Stokes parameter, A is the projection operator mapping the data between the time domain and the map domain, and N is the noise covariance matrix in the time basis. For this work, we employ a naive mapmaking approach where we approximate N as a diagonal matrix with elements equal to the variance of the time segment being mapped, equivalent to one sweep of the telescope. To make this approximation valid for the Stokes I component, we suppress the temperature signal from the atmosphere, which has a $1/f$ spectrum and is correlated between detectors. We do this by fitting a polynomial in the azimuth domain to each timestream and subtracting it. While this biases the large-scale modes in the temperature maps, the fast modulation shifts the linearly and circularly polarized signals up in the frequency domain to a band centered at 10 Hz, where their amplitudes are not attenuated by this filtering. The recovered V map is nearly unbiased (Figure 2).

We have extended the `Ninkasi` mapmaking code written for the Atacama Cosmology Telescope experiment (Dünner et al. 2013) to incorporate Equation (1). We use it to perform all the data operations described in this section and to bin the maps into a `HealPix` grid in equatorial coordinates (Figure 3).

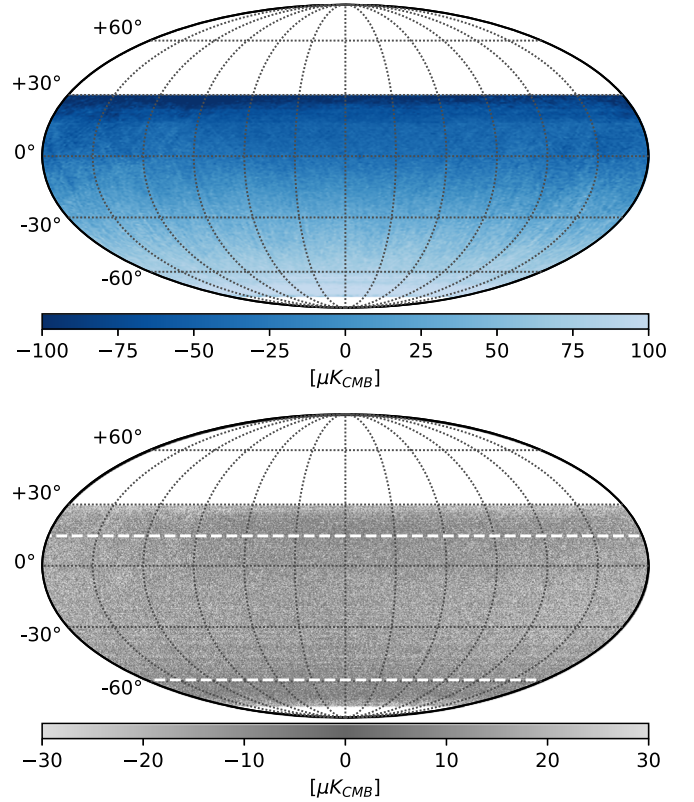


Figure 3. Top: Stokes V map made from 239 days of CLASS data. This map is coadded from the 26 maps used in the cross-spectra analysis of Section 3.2. The gradient-like dipole structure visible in the map is caused by Zeeman emission of atmospheric oxygen, which depends on the inner product of the telescope’s boresight vector and the Earth’s magnetic field vector. This creates a pattern that is approximately only a function of decl. Bottom: Stokes V map coadded from decl.-filtered maps used in the upper-limit analysis. The solid white regions are not observed by the CLASS survey. The area between the white dashed lines is the analysis region.

In this analysis we consider only the Stokes V maps. We use the temperature maps (Stokes I) for calibration of the instrument (Appel et al. 2019). The Stokes Q and U maps will serve as a consistency check to the maps produced by the main linear polarization analysis pipeline, which employs a destriping mapmaker (J. Eimer et al. 2019, in preparation).

Before analyzing each map we discard the edges of the observing region by only keeping pixels visited by every detector, bringing the covered sky fraction to 56%. We perform the analysis on the region of the sphere between declinations of -60° S and 15° N. A correlation analysis between the I and V maps made with this pipeline shows no measurable $I \rightarrow V$ leakage, and therefore we do not apply a galactic mask. We place a 2σ upper limit on the leakage term of 0.03%, implying an upper limit on the expected leakage signal that is two orders of magnitude below the CMB upper limits presented in Section 3.2.

Since CLASS observes at fixed elevation, the circularly polarized atmospheric signal depends only on azimuth. With the telescope’s observing strategy, this time-invariant azimuthal dependence implies a signal in the maps that is approximately independent of R.A. To estimate the power spectrum of the extraterrestrial sky from the maps, we discard modes contaminated by azimuth-synchronous signals by subtracting the mean of the map at each decl. In the next section we describe how we estimate the power spectrum of the maps,

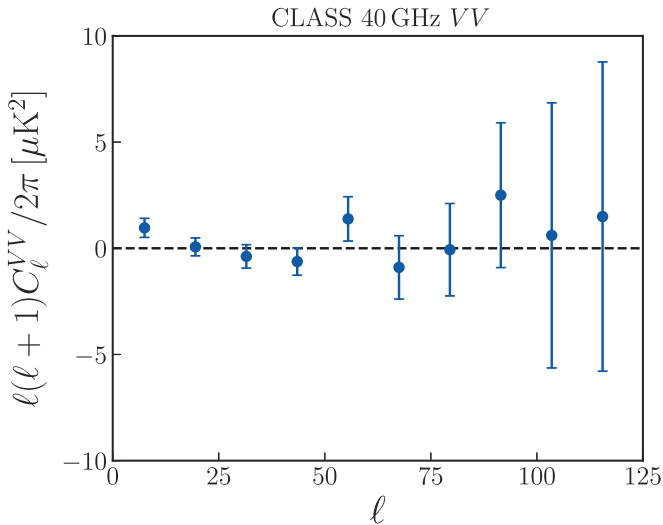


Figure 4. VV power spectrum at 40 GHz after suppression of the atmospheric component, binned into bins with $\Delta\ell = 12$. The data have a reduced- $\chi^2 = 0.921$. Monte Carlo simulations made with the sample bin-bin covariance matrix yield a p -value of 0.54 for the data, indicating no statistically significant detection of power.

taking into account the effects of the time- and map-domain filtering.

2.3. Power Spectrum Estimation

The selected data set consists of 239 constant elevation scans (CES) with the 40 GHz telescope, each between 10 and 24 hr in duration. The average length of one CES is 20 hr, yielding a total of 4772 hr of observation including night and daytime data. We make 26 independent maps with the data distributed so that each map has full coverage of the observation region and similar amounts of integration time. When distributing the data between the maps, we prioritize spatial coverage and map weight over boresight rotation coverage, since, unlike linear polarization, measurements of circular polarization do not require observations at different telescope boresight orientations.

From these maps we produce $\binom{26}{2} = 325$ cross-spectra using the `PolSpice` estimator described in Chon et al. (2004). We use the mean and spread in the distribution of cross-spectra to estimate the bandpowers and their uncertainties. We use ensembles of simulations of an isotropic Gaussian random field with a flat spectrum to check the robustness of the estimator given our sky mask. These results are insensitive to other choices of continuous input spectrum. We use these simulations to verify that `PolSpice` returns unbiased bandpowers in bins with width $\Delta\ell = 12$ starting at $\ell = 1$ for our choice of sky mask. Based on these simulations, we choose to forego the apodization of the correlation function. Since V is a spin-0 field, the treatment follows that of a temperature map.

When computing the power spectra, we weight each map by the VV element of the naive pixel covariance matrix, which is an estimate of the noise in each pixel accounting for integration time and the modulation efficiency of the VPM in V . This map-domain weighting accounts for the inhomogeneity of the noise in the maps and reduces the variance across all bins by $\sim 15\%$.

To characterize the effects of the time- and map-domain filtering, we process a simulation ensemble through our

pipeline. These simulations use the same data selection, observing times, and filtering used to make the data maps. The m -averaged filter transfer function, F_ℓ , quantifying the amount of signal attenuated by the time- and map-domain filtering (described in Section 2.2) is given by the mean of the ratios of the power spectra of the filtered simulated maps to the input simulated maps. The uncertainty in each bin of the transfer function is given by the spread of the distribution of the simulations. The gain of the instrument as a function of multipole is given by the instrument’s beam window function, B_ℓ^2 . The beam window function is based on observations of the Moon, and described in detail in Xu et al. (2019). The product of these two quantities is the power spectrum window function, $W_\ell = F_\ell B_\ell^2$, used to debias the measured bandpowers. We bin this window function in bins with width $\Delta\ell = 12$, the same as the data, to reduce correlations between adjacent multipoles at low ℓ .

Note from Figure 2 that the filtering attenuates at most 14% of the power, in the lowest bin, which spans $1 \leq \ell \leq 12$.

3. Results

We present a new upper limit to extraterrestrial emission of circular polarization at $1 \leq \ell \leq 120$, and the detection of circularly polarized atmospheric emission, both at 40 GHz. The characteristics of the atmospheric emission in particular are of interest to current and future ground-based experiments targeting high-precision polarization measurements at large angular scales.

We check for self-consistency of the maps with a permutation test. From the 26 maps we construct 13 difference maps by randomly drawing pair combinations. We compute all possible cross-spectra from these maps and average them to estimate the null spectrum, and then compute the p -value of this null spectrum from the sample covariance matrix of all the cross-spectra. We repeat this operation 500 times. These 500 p -values are uniformly distributed between zero and one, with no statistically significant outliers, indicating that all observed signal is common to all maps. This rules out statistically significant amounts of time-varying systematic errors that might affect the maps unevenly. A more comprehensive analysis of systematic errors investigating other splits of the data is left for future work.

3.1. Atmospheric Dipole

The main component seen in the maps is the polarized atmospheric emission (Figure 3), caused by the Zeeman transitions of oxygen in the atmosphere as predicted by Keating et al. (1998), Hanany & Rosenkranz (2003), and Spinelli et al. (2011). The Earth’s magnetic field causes a splitting of the energy levels of oxygen in the atmosphere. Transitions between these energy levels are polarized, but have weak to no dependence on time-varying environmental parameters such as precipitable water vapor, temperature, and atmospheric pressure.

In the 40 GHz V map the majority of the atmospheric component is well modeled by a dipole with an amplitude of $124 \pm 4 \mu\text{K}$. This corresponds to a spherical harmonic mode at $(\ell, m) = (1, 0)$ with coefficient $a_{\ell m}$ equal to $a_{10} = 255 \pm 8 \mu\text{K}$. A detailed analysis of this component, including physically motivated atmospheric modeling, is discussed in Petroff et al. (2019).

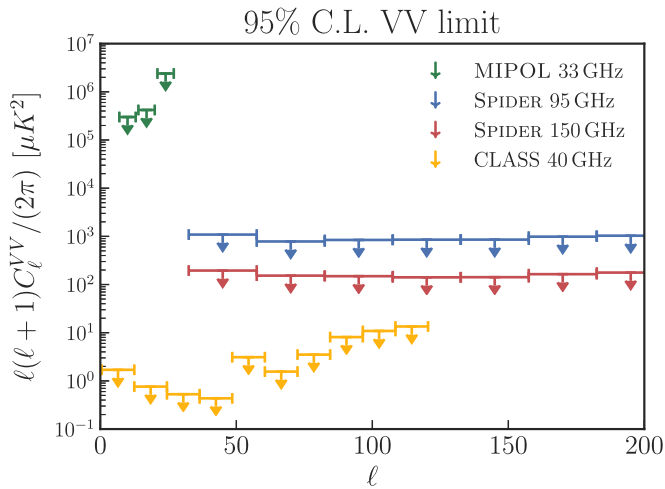


Figure 5. CLASS 95% confidence upper limits to extraterrestrial circular polarization at 40 GHz. The MIPOL (Mainini et al. 2013) limits at 33 GHz, and the SPIDER CMB limits (Nagy et al. 2017) at 95 and 150 GHz, are shown for comparison in the range $1 \leq \ell \leq 200$. The CLASS bins are $\Delta\ell = 12$ wide, starting at $\ell = 1$ and going to $\ell = 120$.

With the contaminated decl.-dependent modes suppressed by the decl. filter we are left with an estimate of the circular polarization coming from the extraterrestrial sky. We model the effects of the filter statistically with Monte Carlo simulations to debias the VV power spectrum, shown in Figure 4. A 95% confidence upper limit is constructed from this spectrum and is shown in Figure 5.

The amplitude of the atmospheric emission is proportional to the inner product of the telescope’s line-of-sight vector and the Earth’s magnetic field vector (Lenoir 1968). A map-domain decl. filter that subtracts the mean along each row of pixels, applied independently to each map in the splits, suppresses the signal below measurable levels (Figure 4). The decl.-filtered maps are used to estimate the power spectrum of the extraterrestrial signal.

Previous work by Hanany & Rosenkranz (2003) concluded that a 0.01% leakage from circular to linear polarization would produce an atmospheric polarization signal larger than the expected B-mode signal for a tensor-to-scalar ratio of $r = 0.01$. The effectiveness of the decl. filter indicates the detected atmospheric signal is confined to the small fraction of modes that are not a function of R.A. Discarding these modes corresponds to a loss of sensitivity of $\sim 1\%$ at $\ell = 80$ (Figure 2), the location of the recombination peak in the B-mode spectrum targeted by most B-mode experiments. The highly localized nature of the contaminated modes relaxes the tolerances for instrumental $V \rightarrow P$ leakage for instruments targeting $r \lesssim 0.01$ from the ground.

3.2. Upper Limit on Emission of Circular Polarization

The error bars plotted in Figure 4 are the square root of the diagonal elements of the bin–bin sample covariance matrix for all 325 cross-spectra, divided by the square root of the number of cross-spectra. Uncertainties from the filter transfer function and beam window function are propagated assuming Gaussianity of the distributions in each bin. This assumption is valid for all bins given the chosen bin width. The data have a reduced- $\chi^2 = 0.921$, which has a p -value of 0.54, indicating no statistically significant detection of power over the multipole range $1 \leq \ell \leq 120$. This p -value is estimated via Monte Carlo

simulations with samples drawn from the sample covariance matrix.

From this power spectrum we produce an upper limit per bin equal to the estimated bandpower value plus a 95% confidence limit, shown in Figure 5. This upper limit is improved by five orders of magnitude over the previous limit at the Ka band by the MIPOL experiment at large scales (Mainini et al. 2013), and by two orders of magnitude over the previously best CMB upper limits by SPIDER (Nagy et al. 2017).

4. Conclusion

We present results on circular polarization from the first two years of observation with the CLASS 40 GHz instrument, consisting of a detection of circularly polarized atmospheric emission and an upper limit on extraterrestrial emission in the range $1 \leq \ell \leq 120$. The atmospheric signal, when measured at 45° elevation, has an amplitude of $124 \pm 4 \mu K$. The upper limit on emission of circular polarization at 40 GHz ranges from 0.4 to $13.5 \mu K^2$ (Figure 5), representing an improvement by two orders of magnitude in the constraint on emission of circular polarization from the CMB, and by five orders of magnitude at the largest scales.






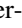
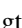
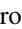


CLASS telescopes covering three additional frequencies—90, 150, and 220 GHz—are currently equipped with VPMs and operating in the Atacama Desert, in Chile. The extended frequency and multipole coverage provided by these instruments will add considerable constraining power to Galactic, extragalactic, and cosmological models of circularly polarized emission.

We acknowledge the National Science Foundation Division of Astronomical Sciences for their support of CLASS under grant Nos. 0959349, 1429236, 1636634, and 1654494. We thank Johns Hopkins University President R. Daniels and Dean B. Wendland for their steadfast support of CLASS. We further acknowledge the very generous support of Jim and Heather Murren (JHU A&S ’88), Matthew Polk (JHU A&S Physics BS ’71), David Nicholson, and Michael Bloomberg (JHU Engineering ’64). The CLASS project employs detector technology developed in collaboration between JHU and Goddard Space Flight Center under several previous and ongoing NASA grants. Detector development work at JHU was funded by NASA grant No. NNX14AB76A. R.R. acknowledges partial support from CATA, BASAL grant AFB-170002, and Conicyt-FONDECYT through grant 1181620. R.D. thanks CONICYT for grant BASAL CATA AFB-170002. We acknowledge scientific and engineering contributions from Max Abitbol, Fletcher Boone, Francisco Espinoza, Connor Henley, Lindsay Lowry, Isu Ravi, Gary Rhodes, Bingie Wang, Zi’ang Yan, Qinan Wang, and Tiffany Wei. We acknowledge productive collaboration with Dean Carpenter and the JHU Physical Sciences Machine Shop team. Part of this research project was conducted using computational resources at the Maryland Advanced Research Computing Center (MARCC). Part of this research project was conducted using computational resources of the Geryon-2 cluster at Centro de Astroingeniería UC. CLASS is located in the Parque Astronómico Atacama in northern Chile under the auspices of the Comisión Nacional de Investigación Científica y Tecnológica de Chile (CONICYT).

Software: IPython (Perez & Granger 2007), numpy (van der Walt et al. 2011), scipy (Virtanen et al. 2019), matplotlib (Hunter 2007), HEALPix (Górski et al. 2005;

Zonca et al. 2019), CAMB (Lewis et al. 2000), GNU Octave (Eaton et al. 2019).

ORCID iDs

Ivan L. Padilla  <https://orcid.org/0000-0002-0024-2662>
 Joseph R. Eimer  <https://orcid.org/0000-0001-6976-180X>
 Yunyang Li
 (李云扬)  <https://orcid.org/0000-0002-4820-1122>
 Graeme E. Addison  <https://orcid.org/0000-0002-2147-2248>
 John W. Appel  <https://orcid.org/0000-0002-8412-630X>
 Charles L. Bennett  <https://orcid.org/0000-0001-8839-7206>
 Ricardo Bustos  <https://orcid.org/0000-0001-8468-9391>
 Manwei Chan  <https://orcid.org/0000-0003-1127-0965>
 David T. Chuss  <https://orcid.org/0000-0003-0016-0533>
 Jullianna Couto  <https://orcid.org/0000-0002-0552-3754>
 Sumit Dahal  <https://orcid.org/0000-0002-1708-5464>
 Thomas Essinger-Hileman  <https://orcid.org/0000-0002-4782-3851>
 Pedro Fluxá  <https://orcid.org/0000-0002-2061-0063>
 Saianeesh K. Haridas  <https://orcid.org/0000-0001-6519-502X>
 Kathleen Harrington  <https://orcid.org/0000-0003-1248-9563>
 Tobias A. Marriage  <https://orcid.org/0000-0003-4496-6520>
 Carolina Núñez  <https://orcid.org/0000-0002-5247-2523>
 Matthew A. Petroff  <https://orcid.org/0000-0002-4436-4215>
 Karwan Rostem  <https://orcid.org/0000-0003-4189-0700>
 Robert W. Stevens  <https://orcid.org/0000-0003-4939-076X>
 Duncan J. Watts  <https://orcid.org/0000-0002-5437-6121>
 Edward J. Wollack  <https://orcid.org/0000-0002-7567-4451>
 Zhilei Xu (徐智磊)  <https://orcid.org/0000-0001-5112-2567>

References

- Appel, J. W., Ali, A., Amiri, M., et al. 2014, *Proc. SPIE*, 9153, 91531J
 Appel, J. W., Xu, Z., Padilla, I. L., et al. 2019, *ApJ*, 876, 126
 Batebi, S., Haghighat, M., Mohammadi, R., et al. 2016, arXiv:1605.09045
 Battistelli, E. S., Amiri, M., Burger, B., et al. 2008, *JLTP*, 151, 908
 Bennett, C. L., Larson, D., Weiland, J. L., et al. 2013, *ApJS*, 208, 20
 BICEP2 Collaboration/Keck Array Collaboration, Ade, P. A. R. 2018, *PhRvL*, 121, 221301
 Carroll, S. M., Field, G. B., & Jackiw, R. 1990, *PhRvD*, 41, 1231
 Chon, G., Challinor, A., Prunet, S., et al. 2004, *MNRAS*, 350, 914
 Chuss, D. T., Wollack, E. J., Henry, R., et al. 2012, *ApOpt*, 51, 197
 Cooray, A., Melchiorri, A., & Silk, J. 2003, *PhLB*, 554, 1
 De, S., & Tashiro, H. 2015, *PhRvD*, 92, 123506
 Dünner, R., Hasselfield, M., Marriage, T. A., et al. 2013, *ApJ*, 762, 10
 Eaton, J. W., Bateman, D., Hauberg, S., & Wehbring, R. 2019, GNU Octave, Version 4.2.0 (London: Samurai Media)
 Eimer, J. R., Bennett, C. L., Chuss, D. T., et al. 2012, *Proc. SPIE*, 8452, 845220
 Ejlli, D. 2019, *EPJC*, 79, 231
 Essinger-Hileman, T., Ali, A., Amiri, M., et al. 2014, *Proc. SPIE*, 9153, 91531I
 Gandilo, N., Ade, P., Benford, D. J., et al. 2017, AAS Meeting, 229, 430.04
 Giovannini, M. 2009, *PhRvD*, 80, 123013
 Giovannini, M. 2010, *PhRvD*, 81, 023003
 Górski, K. M., Hivon, E., Banday, A. J., et al. 2005, *ApJ*, 622, 759
 Haghighat, M., Mahmoudi, S., Mohammadi, R., et al. 2019, arXiv:1909.03883
 Hanany, S., & Rosenkranz, P. 2003, *NewAR*, 47, 1159
 Harrington, K., Eimer, J., Chuss, D. T., et al. 2018, *Proc. SPIE*, 10708, 107082M
 Harrington, K., Marriage, T., Ali, A., et al. 2016, *Proc. SPIE*, 9914, 99141K
 Henning, J. W., Sayre, J. T., Reichardt, C. L., et al. 2018, *ApJ*, 852, 97
 Hunter, J. D. 2007, *CSE*, 9, 90
 Inomata, K., & Kamionkowski, M. 2019, *PhRvD*, 99, 043501
 Kamionkowski, M. 2018, *PhRvD*, 97, 123529
 Keating, B., Timbie, P., Polnarev, A., et al. 1998, *ApJ*, 495, 580
 King, S., & Lubin, P. 2016, *PhRvD*, 94, 023501
 Kovac, J. M., Leitch, E. M., Pryke, C., et al. 2002, *Natur*, 420, 772
 Legg, M. P. C., & Westfold, K. C. 1968, *ApJ*, 154, 499
 Lenoir, W. B. 1968, *JGR*, 73, 361
 Lewis, A., Challinor, A., & Lasenby, A. 2000, *ApJ*, 538, 473
 Louis, T., Grace, E., Hasselfield, M., et al. 2017, *JCAP*, 06, 031
 Mainini, R., Minelli, D., Gervasi, M., et al. 2013, *JCAP*, 08, 033
 Miller, N. J., Chuss, D. T., Marriage, T. A., et al. 2016, *ApJ*, 818, 151
 Mohammadi, R. 2013, arXiv:1312.2199
 Montero-Camacho, P., & Hirata, C. M. 2018, *JCAP*, 08, 040
 Motie, I., & Xue, S.-S. 2011, arXiv:1104.3555
 Nagy, J. M., Ade, P. A. R., Amiri, M., et al. 2017, *ApJ*, 844, 151
 Netterfield, C. B., Ade, P. A. R., Bock, J. J., et al. 2002, *ApJ*, 571, 604
 Perez, F., & Granger, B. E. 2007, *CSE*, 9, 21
 Petroff, M. A., Eimer, J. R., Harrington, K., et al. 2019, arXiv:1911.01016
 Planck Collaboration, Akrami, Y., Arroja, F., et al. 2018, A&A, in press (arXiv:1807.06205)
 Sawyer, R. F. 2015, *PhRvD*, 91, 021301
 Spinelli, S., Fabbian, G., Tartari, A., et al. 2011, *MNRAS*, 414, 3272
 van der Walt, S., Colbert, S. C., & Varoquaux, G. 2011, *CSE*, 13, 22
 Venumadhav, T., Oklopčić, A., Gluscevic, V., et al. 2017, *PhRvD*, 95, 083010
 Virtanen, P., Gommers, R., Oliphant, T. E., et al. 2019, arXiv:1907.10121
 Watts, D. J., Larson, D., Marriage, T. A., et al. 2015, *ApJ*, 814, 103
 Watts, D. J., Wang, B., Ali, A., et al. 2018, *ApJ*, 863, 121
 Xu, Z., Brewer, M. K., Fluxa, P., et al. 2019, arXiv:1911.04499
 Zarei, M., Bavarsad, E., Haghighat, M., et al. 2010, *PhRvD*, 81, 084035
 Zonca, A., Singer, L., Lenz, D., et al. 2019, *JOSS*, 4, 1298